On-Chip Infrared Spectroscopic Sensing: Redefining the Benefits of Scaling

Derek M. Kita, Hongtao Lin, Anu Agarwal, Kathleen Richardson, Igor Luzinov, Tian Gu,
and Juejun Hu, *Member, IEEE*

(Invited Paper)

Abstract—**Infrared (IR) spectroscopy is widely recognized as a gold standard technique for chemical analysis. Recent strides in photonic integration technologies offer a promising route towards enabling miniaturized, rugged platforms for IR spectroscopic analysis. Here we show that simple size scaling by replacing bulky discrete optical elements used in conventional IR spectroscopy with their on-chip counterparts is not a viable route for on-chip infrared spectroscopic sensing, as it cripples the system performance due to the limited optical path length accessible on a chip. In this context, we discuss two novel photonic sensor designs uniquely suited for microphotonic integration. We leverage strong optical and thermal confinement in judiciously designed microcavities to circumvent the thermal diffusion and optical diffraction limits in conventional photothermal sensors and achieve parts-per-billion level gas molecule limit of detection. In the second example, an on-chip spectrometer design with Fellgett's advantage is proposed for the first time. The design enables sub-nm spectral resolution on a millimeter-sized, fully packaged chip without mechanical moving parts.**

Index Terms—**Chemical sensors, infrared sensors, optical sensors, optical resonators, photothermal effects, spectroscopy.**

I. INTRODUCTION: THE CASE FOR ON-CHIP INFRARED SENSING

INFRARED spectroscopy probes the phonon vibrational states of molecules by measuring wavelength-dependent optical absorption in the mid-infrared regime (2.5–25 μm wavelength or 400–4,000 cm^{-1} in wavenumber). IR spectroscopy is widely recognized as the gold standard for chemical analysis given its superior specificity: molecular species can be uniquely identified with their characteristic optical absorption bands. Such a "fingerprinting" capability makes IR spectroscopy an ideal technology for applications involving chemical analysis in complex environments, such as industrial process control, environmental monitoring, food quality assessment, forensics, and remote sensing [1].

Traditional IR spectroscopy relies on bench-top instruments such as Fourier Transform Infrared (FTIR) spectrometers located in dedicated laboratories. These instruments are of the size of large desktop computers and easily cost over $100K. Further, robustness of these systems is often compromised by fragile mechanical moving parts or stringent optical alignment requirements. To meet the increasing demands of field-deployed applications, a number of portable spectrometer products have been successfully developed by miniaturizing the discrete optical components used in their bench-top counterparts [2]. The vast majority of these products, however, are designed for the visible and near-IR wavelengths (<2.5 μm) where high-performance, low-cost photodetector arrays are readily available. Portable systems operating in the mid-IR range where the characteristic absorption bands of most molecules reside are still limited in terms of size, performance, and cost.

On-chip photonic integration offers an attractive solution to overcoming the aforementioned limitations associated with bench-top or current portable spectroscopic sensing systems. In addition to the apparent advantages in size, weight, and power (SWaP), no optical alignment is necessary between lithographically defined components in integrated photonic modules, thereby improving both manufacturing throughput and system ruggedness. Planar photonic integration further opens up the possibility of cost reduction leveraging standard high-volume semiconductor manufacturing processes for applications such as consumer electronics or sensor networks for the internet of things (IoT).

The photonic integration approach also comes with its own pitfalls. In particular, on-chip sensors are often associated with an optical path length much smaller than their bulk counterparts. Despite improved coupling efficiencies between individual on-chip components, the small physical size of a typical photonic integrated circuit (PIC) and large optical propagation losses ultimately limit the accessible optical path length. Along this line, Section II analyzes performance evolution trends as sensor footprint reduces and points to key performance limitations arising from such size down-scaling. Sections III and IV are then dedicated to two novel on-chip device designs capable of circumventing these limitations.

II. PERFORMANCE SCALING IN CHIP-SCALE SPECTROSCOPIC SENSING SYSTEMS

There are two basic system configurations for infrared spectroscopic sensing. In a "laser-scanning" sensing system, a tun-
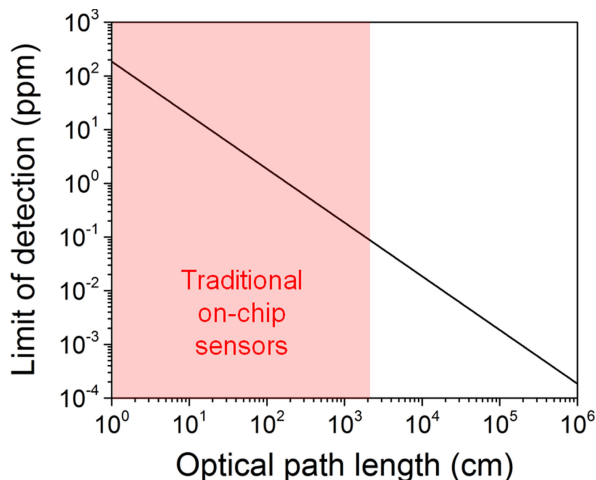
Fig. 1. Spectroscopic sensor limit of detection (in terms of volumetric gas concentration) as a function of optical path length, assuming a detector noise floor of 0.1% and a molecular absorption cross section of 10^{-18} cm^2. The region in red represents accessible optical path lengths for on-chip sensors assuming a record low loss of 0.045 dB/m (in Si$_3$N$_4$ waveguides [4]) and a confinement factor in the sensing region of 0.2.
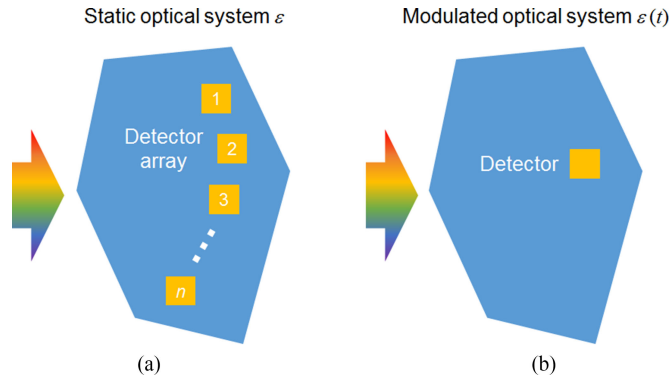

Fig. 2. Generic spectrometer models: a single mode polychromatic input is launched into an optical system and its spectral content is quantified via the detector output. In (a) the "dispersive" type configuration, the optical system is time-independent and a detector array is used to collect spatially "coded" spectral information; in (b) the "modulated" type design, the optical system is modulated and the resulting time-dependent single-element detector output is used to extract the spectral information.

able, narrow-line-width laser is coupled to a sensing element (e.g. waveguide evanescent sensors) where optical absorption by the analyte takes place. A single-element detector is used to record the spectrum as the laser wavelength is swept across the target spectral range. Alternatively, the "spectrometric" approach employs a broadband source in conjunction with a spectrometer to resolve the wavelength-dependent absorption in the sensing element. In this section, we show that key sensor performance metrics in both configurations (limit of detection in the former case and spectral resolution in the latter case) scale inversely with the effective optical path length. As a consequence, simple size down-scaling of conventional spectroscopic sensor designs to the chip-scale severely degrades the sensor performance often to an unacceptable level.

A. Detection Limit in a Laser-Scanning Sensing System

Assuming that the Lambert-Beer law holds across the entire analyte concentration range [3], optical absorbance of the analyte scales linearly with the target molecule concentration. In the following simple example, we assume a detector noise floor of 0.1% at some given sampling bandwidth, a molecular absorption cross section of 10^{-18} cm^2 (a typical value for molecules in the mid-infrared), that gas samples are held at 300 K and 1 atm, and that the detection limit corresponds to a signal-to-noise ratio (SNR) of unity. The limit of detection in terms of volumetric gas concentration in parts-per-million (ppm) is plotted as a function of optical path length in Fig. 1.

Since propagation loss of on-chip optical waveguides is generally around 0.1 to a few dB/cm, the detection limit of traditional on-chip sensors is bound to the ppm level. We further note that using resonant cavity structures does not contribute to improving the limit of detection, since the effective optical path length in resonant cavities is similarly bound by optical propagation loss. The limited path length accounts for the vast performance gap between on-chip infrared spectroscopic sensors and free-space absorption cells (e.g. Herriott cells [5]), as the latter can achieve optical path lengths exceeding hundreds of meters and hence ppb-level detection.

B. Performance Scaling in a Spectrometric System

Compared to laser-scanning systems, spectrometric sensors claim the advantages of broad spectral bandwidth not limited by the gain spectrum of laser media, and are thus particularly suited for chemical analysis in a complex environment.

Fig. 2 illustrates two types of spectrometer configurations. In both configurations, a single-spatial-mode polychromatic optical input is launched into a generic linear and source-free optical system, which is characterized by a spatial distribution of dielectric constant $\epsilon(x)$. In the "dispersive" design, the polychromatic input generates a spatially and wavelength dependent electric field complex amplitude $E(x, \lambda)$. A photodetector array probes the spatial field distribution and converts it into spectral information of the optical input via a linear transformation. Classical dispersive spectrometers using diffractive gratings, prisms, or resonant cavity arrays as the spectrum-splitting elements fall in this category [6]–[14]. Furthermore, the generalized "dispersive" spectrometers shown in Fig. 2(a) also encompass those based on the wavelength multiplexing principle, which date back to the static multi-slit design conceived by Golay in the 1940's [15] and have also garnered considerable interest recently [16]–[23]. The latter configuration illustrated in Fig. 2(b) applies a time-dependent modulation to the optical system such that its dielectric function $\epsilon(x, t)$ is both spatially and temporally varying. Modulation of the dielectric function modifies the electric field distribution $E(\lambda, t)$ at the single-element detector, from which the spectrum of incident light can be inferred through a linear transformation to map the light intensity values measured by the detector from the time domain to the spectral domain. Compared to the "dispersive" type spectrometers, properly designed time-domain "modulated" systems feature the Fellgett or multiplexing advantage, as the input light is collected by one (or two) photodetectors rather than being split between a large number of detectors. As a result, the SNR is enhanced by a factor

of $\sqrt{N}/2$ for the same integration time, where N is the number of spectral channels or data points [24], [25]. Such time-domain modulation can be implemented via mechanical motion of optical components, for instance in the cases of FTIR spectrometers. Alternative modulation methods making use of electro-optic and thermo-optic effects have also been demonstrated [26]–[28].

Similar to laser-scanning systems, the detection limit of spectrometric sensors is also determined by the accessible optical path length in the sensing element. Spectral resolution $\delta\lambda$ (defined as the minimum resolvable wavelength difference) and bandwidth are two other important metrics.

Spectral resolution of both "dispersive" and "modulated" spectrometers scales inversely with the effective optical path length in the optical system. For optical systems with a deterministic optical path, the path length is proportional to the system linear dimension. For optical systems consisting of random scattering media, the effective path length scales with the square root of the system size [15]. It is therefore apparent that direct size down-scaling is not a preferred solution for spectrometer miniaturization and on-chip integration due to the deteriorating spectral resolution. In addition to optical path length, spectral resolution is also determined by the optical systems "dispersive power" (generally defined as $d|E(x)|/d\lambda$, which applies to wavelength multiplexed spectrometers as well) in a "dispersive" spectrometer, whereas in a "modulated" system, $\delta\lambda$ is inversely proportional to the modulation amplitude $\Delta\epsilon_{\max}$.

Spectral bandwidth of spectrometers, in general, equals the product of the number of spectral channels N and the spectral resolution $\delta\lambda$. Here N can also be interpreted as the number of useful detector elements in the "dispersive" configuration or distinctive optical states $\epsilon(x, t)$ in the "modulated" scheme. In practice, the spectrometer bandwidth is often constrained by light source bandwidth or single-mode condition of the photonic components used to construct the spectrometer.

III. CHIP-SCALE OPTICAL CAVITY ENHANCED PHOTOTHERMAL SPECTROSCOPY

The sensitivity of on-chip cavity-enhanced sensors is fundamentally limited by high waveguide losses as we discussed in Section II. Traditional on-chip microcavity absorption spectrometers measure the change in complex refractive index, the sensitivity of which is largely limited by scattering loss from cavity sidewall roughness [29]–[34]. In order to achieve sensitivities comparable to state-of-the-art benchtop spectroscopy instruments, on-chip sensors must exploit unique properties of their reduced size and waveguiding materials. In this section, we describe a method of performing photothermal spectroscopy to detect trace gases at the part-per-billion level (ppb). Photothermal spectroscopy has been predicted as a technique 10^4 times more sensitive than conventional microcavity absorption spectroscopy [35], [36]. We propose a new technique that monitors the shift in cavity resonance as a result of heating. Resonant absorption of cavity light by the gas molecules thermally heats the cavity, producing a large resonant shift in a suitably designed microdisk cavity.
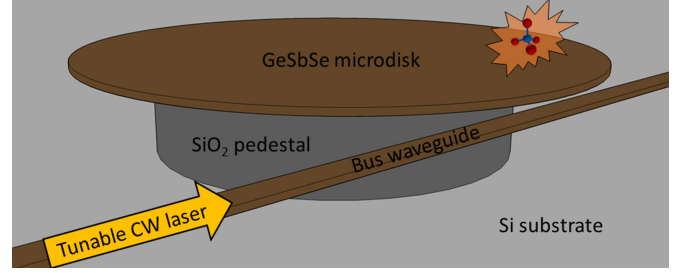

Fig. 3. Schematic of a suspended microdisk cavity structure for sensing a target gas molecule in the surrounding air. Brown denotes a 30 μm radius $Ge_{23}Sb_7Se_{70}$ microdisk coupled to a bus waveguide, all suspended 10 μm above a Si substrate by SiO_2 supports.

Fig. 4. Simulated transmission spectra for a bus-waveguide coupled to a microcavity in the presence of heating from intrinsic optical absorption (by the cavity) $\alpha_{\mathrm{int}} = 10^{-4}\,\mathrm{cm}^{-1}$ and external optical absorption $\alpha_{\mathrm{ext}} = 10^{-5}\,\mathrm{cm}^{-1}$ (blue curve) and $\alpha_{\mathrm{ext}} = 9 \times 10^{-5}\,\mathrm{cm}^{-1}$ (red curve). Input light is scanned from short to long wavelengths.

A. Resonant Shifts in Heated Microcavities

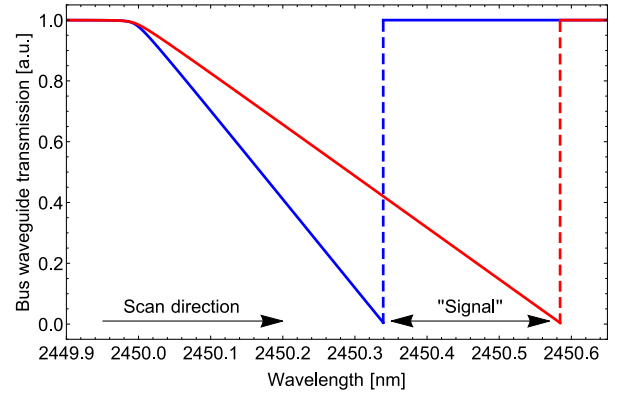In this section we consider a microdisk such as the one shown in Fig. 3 coupled to a bus waveguide that delivers light of wavelength λ_p and power I into the cavity. Fig. 4 plots simulated transmission spectra for a bus-waveguide coupled to a microcavity in the presence of heating from intrinsic optical absorption $\alpha_{\mathrm{int}} = 10^{-4}\,\mathrm{cm}^{-1}$ and two different external optical absorptions $\alpha_{\mathrm{ext}} = 10^{-4}\,\mathrm{cm}^{-5}$ (blue curve) and $\alpha_{\mathrm{ext}} = 9 \times 10^{-4}\,\mathrm{cm}^{-5}$ (red curve). When input light of wavelength λ_p scans across a cavity resonance from short to long wavelengths, the cavity begins to heat, inducing a red shift in the cavity resonance assuming a positive thermo-optic coefficient. Maximum power is coupled into the cavity when the pump wavelength λ_p is equal to the heated-cavity resonance:

$$\lambda_{p,\min} = \lambda_0(1 + a\Delta T) \qquad (1)$$

where λ_0 is the cold-cavity resonant wavelength and $a \equiv \frac{1}{n_g}\frac{dn_{\mathrm{eff}}}{dT} + a_L$ describes the shift in resonance due to thermal expansion (a_L) and index change (n_g is the group index, and n_{eff} is the effective index). Continuing to scan the pump wavelength past this point results in less cavity heating and a subsequent blue-shift of the cavity resonance. The system relaxes to its off-resonant cold-cavity state at a rate equal to the

system's thermal relaxation time. This behavior is illustrated in Fig. 4 for a cavity in the presence of intrinsic absorption by the cavity material and absorption by gas molecules at one of the cavity's resonant wavelengths. An important assumption of this model is that the analyte's absorption spectrum is relatively slow varying during this laser scanning operation. The change in transmission minima, or $\lambda_{p,\min}$, is related to the absorption coefficient and absorption cross-section of the gas molecules as shown in the following analysis. We would like to note that a full description of the microcavity stability criterion was fully analyzed by Carmon *et al.* [37], and is the basis for this analysis.

B. Analytical Model of Photothermal Sensing

In thermal equilibrium, the heat flowing into a microcavity matches the heat flowing out. The following equation describes the steady state rise in cavity temperature ΔT as a result of photothermal heating assuming a Lorentzian resonance line shape:

$$\frac{I_h}{1 + \left(\frac{\lambda_p - \lambda_0(1+a\Delta T)}{\Delta\lambda/2}\right)^2} = \kappa\Delta T. \tag{2}$$

Here λ_0 is the cold-cavity resonant wavelength, ΔT is the temperature change of the cavity mode, and $\Delta\lambda$ is the resonance bandwidth. Here κ is the lumped thermal conductance between the cavity's optical mode volume and the environment, and is approximated in later sections as the thermal power generated from optical absorption divided by the temperature rise of the optical mode volume. This parameter must be numerically evaluated for a given resonator structure, gas environment, gas flow rate, and optical mode profile. I_h describes the net heat flux flowing into the cavity on resonance, and is the sum of the photothermal heat generated by absorption in the cavity material and the photothermal heat generated by molecules surrounding the cavity:

$$I_h = I\eta\frac{Q}{Q_{\mathrm{int}}} + I\eta f\frac{Q}{Q_{\mathrm{ext}}} \tag{3}$$

where I is the input optical power, η is the coupling efficiency, Q is the intrinsic quality factor, Q_{int} is the quality factor from absorption inside the cavity material, and Q_{ext} is the quality factor from external absorption by gas molecules in the air. The term f describes the fraction of heat generated outside the cavity that contributes to heating the mode volume located primarily inside the cavity core. Expressed in terms of the absorption coefficients, the useful power is:

$$I_h = I\eta\frac{\Gamma_{\mathrm{core}}\alpha_{\mathrm{int}} + f\Gamma_{\mathrm{clad}}\alpha_{\mathrm{ext}}}{\alpha_s + \Gamma_{\mathrm{core}}\alpha_{\mathrm{int}} + \Gamma_{\mathrm{clad}}\alpha_{\mathrm{ext}}}. \tag{4}$$

The denominator is the total absorption seen by light in the cavity, while the numerator considers any absorption that contributes to cavity heating. Here α_s denotes scattering loss, α_{int} denotes intrinsic material absorption, α_{ext} denotes external loss from gas absorption, and Γ represents the modal confinement factors in core and cladding regions. It is important to note that this model neglects the contributions of temperature rise in the air cladding due to air's low thermo-optic coefficient, $dn/dT \sim 10^{-6}$ K^{-1} [38]. Since we are only concerned with the change in

cavity resonance, where $\lambda_p = \lambda_{p,\min}$, (2) simplifies to:

$$I_h = \kappa\Delta T. \tag{5}$$

Further substitution from (1) and (4) results in an equation that relates the peak-shift $\lambda_{p,\min}$ to the equilibrium gas concentration via α_{ext}:

$$I\eta\frac{\Gamma_{\mathrm{core}}\alpha_{\mathrm{int}} + f\Gamma_{\mathrm{clad}}\alpha_{\mathrm{ext}}}{\alpha_s + \Gamma_{\mathrm{core}}\alpha_{\mathrm{int}} + \Gamma_{\mathrm{clad}}\alpha_{\mathrm{ext}}} = \frac{\kappa}{a}\left(\frac{\lambda_{p,\min}}{\lambda_0} - 1\right). \tag{6}$$

The sensitivity of the photothermal gas sensor is the derivative of the peak shift with respect to absorption coefficient α_{ext}, given below in (7):

$$\frac{d\lambda_{p,\min}}{d\alpha_{\mathrm{ext}}} = \frac{I\eta\lambda_0 a\Gamma_{\mathrm{clad}}}{\kappa}\left[\frac{f\alpha_s - (1-f)\Gamma_{\mathrm{core}}\alpha_{\mathrm{int}}}{(\alpha_s + \Gamma_{\mathrm{core}}\alpha_{\mathrm{int}} + \Gamma_{\mathrm{clad}}\alpha_{\mathrm{ext}})^2}\right]. \tag{7}$$

(7) applies when $\alpha_s \gg \alpha_{\mathrm{ext}}$, in which case the change of waveguide-to-cavity coupling is negligible. In the limit of low gas concentrations, α_{ext} becomes negligible and we can further reduce (7) to:

$$\frac{d\lambda_{p,\min}}{d\alpha_{\mathrm{ext}}} = \frac{I\eta\lambda_0 a\Gamma_{\mathrm{clad}}}{\kappa}\left[\frac{f}{\alpha_s + \Gamma_{\mathrm{core}}\alpha_{\mathrm{int}}}\right.$$
$$\left. - \frac{\Gamma_{\mathrm{core}}\alpha_{\mathrm{int}}}{(\alpha_s + \Gamma_{\mathrm{core}}\alpha_{\mathrm{int}})^2}\right]. \tag{8}$$

The term proportional to f in (8) corresponds to the heating of the cavity due to resonant absorption by gas molecules, while the second term proportional to $\Gamma_{\mathrm{core}}\alpha_{\mathrm{int}}$ is physically the desensitization that occurs when more light is absorbed by the cavity core than the external gas molecules. This desensitization is typically insignificant except when α_{int} is greater than α_s, which is rarely the case in on-chip waveguides and cavities (note that Rayleigh scattering in glasses is also part of α_s since Rayleigh scattering does not contribute to heating). The thermal conductance κ and heating ratio f in (8) can be numerically evaluated to provide quantitative prediction of the photothermal dynamic behavior of the cavity.

C. Numerical Modeling of Photothermal Sensing

In this section, we fully describe a prototypical design of a photothermal gas sensor, numerically compute its sensitivity, and compare the numerical results with the analytical model described in the previous subsection. Here we use HF gas as the target analyte, which has strong absorption lines in the 2.4–2.5 μm region and an absorption linewidth roughly two orders of magnitude larger than our microcavity's resonance linewidth at 1 atm [39]. The modeling approach is however generic and can be readily adapted to photothermal sensors operating on other wavelengths.

The sensor geometry is a pedestal microdisk cavity with 60 μm diameter, as shown in Fig. 3. The cavity is fabricated from a high-index chalcogenide glass material for its low thermal conductivity and high photothermal figure of merit. Specifically, we will consider $Ge_{23}Sb_7Se_{70}$ which has a high index ($n = 2.6$ at 2.5 μm), is transparent between 1 and 15 μm wave-
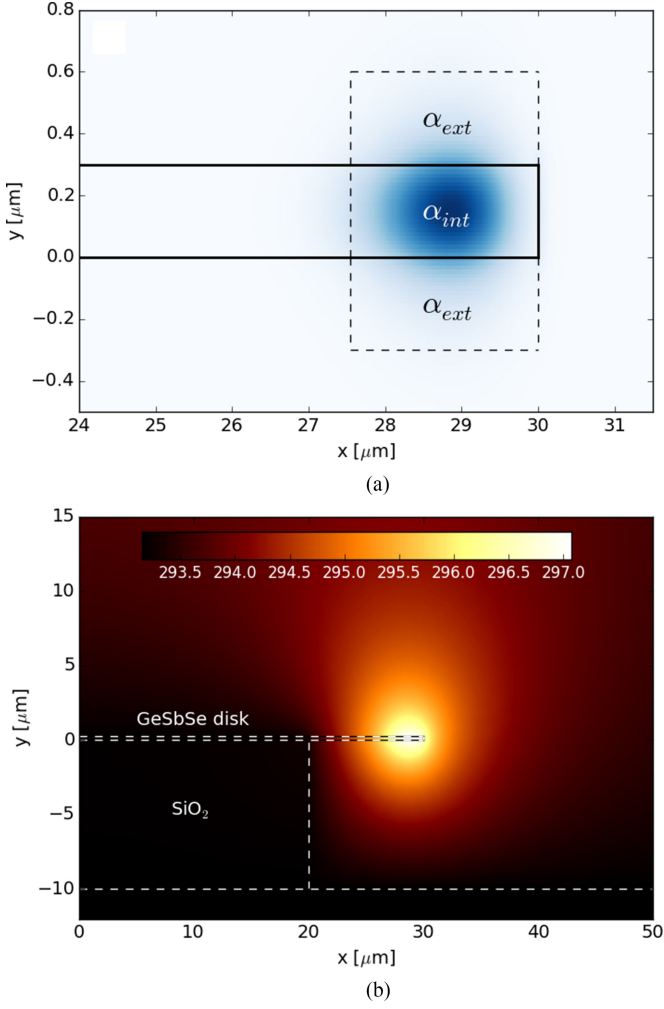
(a)

(b)

Fig. 5. (a) Cross-sectional profile of $|E|^2$ for the resonant cavity mode. (b) Steady state temperature profile in Kelvin of microdisk resonator for an intrinsic absorption of $\alpha_{\text{int}} = 10^{-4}$ cm^{-1}, external absorption of $\alpha_{\text{ext}} = 10^{-5}$ cm^{-1}, scattering loss of $\alpha_s = 0.023$ cm^{-1} and 10 mW input power in the cavity.

lengths, and has a low thermal conductivity of 0.22 W/mK [40]. In the following, we only consider the effects of index change, such that $a = \frac{1}{n_g}\frac{dn_{\text{eff}}}{dT}$. For materials of positive thermal expansion coefficients, such as GeSbSe, the sensitivity will only be further enhanced by incorporating effects of volumetric thermal expansion. The chalcogenide glass cavity can be fabricated by thermal evaporation and lithographic patterning can be achieved by liftoff or reactive-ion etching. The cavity is air-clad to decrease thermal conductance and supported by the 10 μm tall SiO$_2$ pedestal with radius of 20 μm on a Si substrate.

To model the steady-state thermal properties of this system, we constructed a radially symmetric pedestal microdisk structure using the COMSOL Multiphysics package at room temperature with the following simulation parameters: 10 cm/s airflow, GeSbSe density of 4.525 g/cm^3, GeSbSe heat capacity of 0.285 J/(g·K), and material properties for Si, SiO$_2$, and air as defined in the built-in COMSOL material library. Next, we assumed a heat source with input power p_{int} and p_{ext} for the mode

regions inside and outside the disk core as shown in Fig. 5(a).

$$p_{\text{int}} = I\eta\frac{\Gamma_{\text{core}}\alpha_{\text{int}}}{\alpha_s + \Gamma_{\text{core}}\alpha_{\text{int}} + \Gamma_{\text{clad}}\alpha_{\text{ext}}} \quad (9)$$

$$p_{\text{ext}} = I\eta\frac{\Gamma_{\text{clad}}\alpha_{\text{ext}}}{\alpha_s + \Gamma_{\text{core}}\alpha_{\text{int}} + \Gamma_{\text{clad}}\alpha_{\text{ext}}}. \quad (10)$$

We note that in (10) the factor f is absent, since the thermal transport modeling implicitly takes into account the heating ratio. Here, Γ_{core} is calculated from the mode cross-sectional profile via [41]:

$$\Gamma_{\text{core}} = \frac{n_{\text{core}}c_0\epsilon_0 \iint_{\text{core}} |\vec{E}|^2 dxdy}{\iint_\infty \text{Re}(\vec{E} \times \vec{H}^*) \cdot \hat{z} \cdot dxdy}. \quad (11)$$

Γ_{clad} is solved using a formally similar equation where the quantities relevant to the core region in (10) are replaced with those associated with the cladding instead. The scattering absorption coefficient was taken to be 0.1 dB/cm (0.023 cm^{-1}), which represents a microdisk cavity of $Q \sim 10^6$, consistent with our recent report of high-Q chalcogenide glass micro-resonators [42]. The internal absorption coefficient and in-coupled power $I\eta$ were varied as a function of external absorption coefficient to determine the sensitivity of the photothermal sensor. The cross-section of the steady-state thermal distribution was interpolated to fit the same mesh from the mode calculations (performed using Lumerical FDTD). The shift in resonant frequency as a function of this temperature rise was computed using first-order cavity perturbation theory:

$$\Delta\omega = -\frac{\omega}{2}\frac{\iint d^2r[(2n\frac{dn}{dT}\Delta T)|\vec{E}(r)|^2]}{\iint d^2r(\epsilon(r)|\vec{E}(r)|^2)} \quad (12)$$

Finally, the gas concentration detection limit is estimated from the HF absorption cross section at 2.45 μm, 7×10^{-18} cm^2/molecule [43] and assuming that system temperature fluctuations of $\Delta T_{\text{res}} = 0.1$ °C/$\sqrt{\text{Hz}}$ set the lower limit for wavelength resolution:

$$\Delta\lambda_{\text{res}} = \frac{a\Gamma_{\text{core}}\Delta T_{\text{res}}}{n_g} \cdot \lambda_0. \quad (13)$$

Here the group index $n_g = 3.144$ was calculated from experimental ellipsometry data of thin film GeSbSe and via mode simulations.

The results of these computations are shown in Figs. 6 and 7 for varying power and intrinsic absorption coefficients. We note that the main approximation made in the cavity perturbation theory results is the box-shaped heat sources. However, we anticipate this approximation to be small, since the temperature profile is relatively slow varying compared to the electromagnetic mode profile, as shown in Fig. 5(b). From these results, we can see that the analytical expression for photothermal sensitivity given in (7) accurately predicts the power-dependence of the sensor. At modest input powers, detection on the 10's of ppb level is readily attainable. Fig. 7 shows the impact of intrinsic glass material absorption on the detection limit as a result of the desensitization factor in (8). Fig. 7 shows agreement in sensor performance in the limit of low intrinsic material absorption. As the intrinsic material absorption increases, the
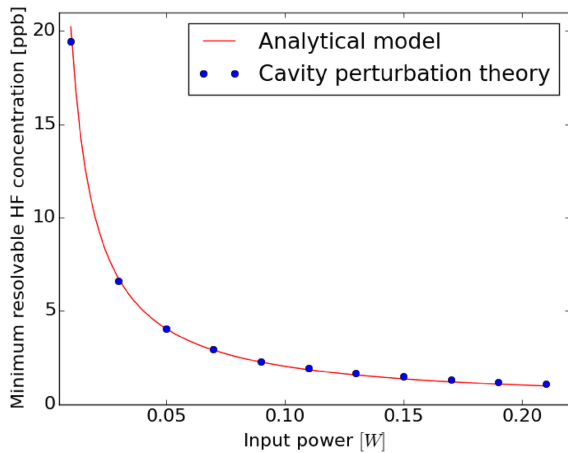
Fig. 6. Minimum resolvable concentration of HF gas molecules given as a function of the input power ($I\eta$) in the cavity given by the analytical model in (7) (red) and from cavity perturbation theory (blue), with $\alpha_{\text{int}} = 10^{-4}$ cm^{-1}.
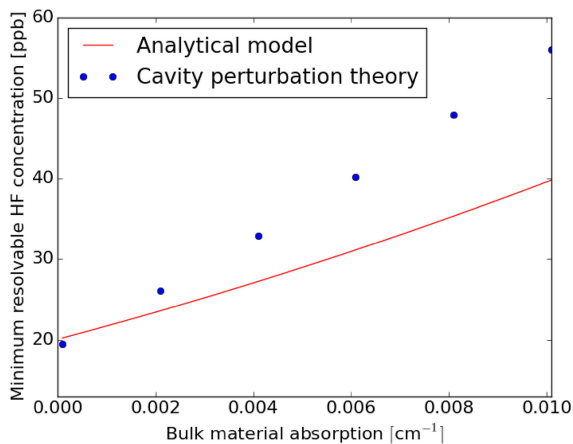

Fig. 7. Minimum resolvable concentration of HF gas molecules given as a function of the bulk cavity material absorption α_{int} given by the analytical model in (7) (red) and from cavity perturbation theory (blue). The analytical model assumes a constant thermal conductance κ, resulting in larger errors as the ratio of heating inside versus outside the cavity changes.

SNR is reduced and the thermal conductance is also modified since the ratio of heat generated in the cavity core versus clad changes. In practice, the desensitization effect is likely insignificant according to the simulation results, because infrared optical attenuation in chalcogenide glass optical fibers is typically less than 1 dB/m (0.0023 cm^{-1}) [44] and the actual material absorption in chalcogenides must be even lower since fiber attenuation also includes contributions from Rayleigh scattering.

In the above analysis, we have demonstrated that monitoring cavity heating as a result of resonant absorption from gas molecules is a viable method of ultrasensitive chemical detection. With modest design parameters and a microcavity designed for maximum thermal isolation, we have demonstrated the feasibility for on-chip gas sensing at a level comparable to the most sensitive free space optical sensors such as Herriott cells. By taking advantage of unique system and material properties at chip-scale dimensions (such as high thermal confinement), it is possible to circumvent large sensitivity penalties that arise from device down-sizing in traditional microcavity spectrometers.

TABLE I
COMPARISON OF OPTICAL PATH LENGTH MODULATION METHODS FOR
ON-CHIP FOURIER TRANSFORM INFRARED SPECTROSCOPY

Modulation mechanism	Modulation efficiency [rad/cm]	Spectral resolution $\delta\lambda$ [nm] for a 1 cm long device at $\lambda = 1.55\ \mu$m
Carrier plasma dispersion [46]	13	N/A
Thermo-optic effect in Si [47]	433	22
Liquid crystal clad waveguide [48]	1,578	6.15
MEMS movable mirror	40,500	0.24
Modification of waveguide path	93,200	0.1

IV. DIGITAL FOURIER TRANSFORM INFRARED SPECTROSCOPY

As discussed in Section II, the "modulated" type spectrometers claim the Fellgett advantage, which underlies their significantly improved SNR over that of the "dispersive" type instruments. The "modulated" type spectrometers are therefore better suited for infrared spectroscopy, as infrared detectors generally exhibit much inferior SNR compared to their counterparts operating at visible wavelengths (in particular, Si photodiodes). Furthermore, the "modulated" type spectrometers can operate with single-element detectors, which is a far more cost-effective option than linear arrays or 2-D imaging arrays required for dispersive spectrometers.

FTIR is perhaps the most common "modulated" type of spectroscopic technique. The basic configuration of an FTIR spectrometer consists of an interferometer with one arm of variable optical path length. According to the Rayleigh criterion, the spectral resolution of an FTIR spectrometer is determined by the path length change ΔL of the variable arm:

$$\delta\nu = \frac{1}{\Delta L} \qquad (14)$$

in wavenumbers, or:

$$\delta\lambda = \frac{\lambda^2}{\Delta L} \qquad (15)$$

in wavelength, where $\delta\lambda$ is the center wavelength. Both (14) and (15) are consistent with our general conclusion that the spectral resolution of "modulated" type spectrometers is inversely proportional to the modulation amplitude.

In conventional FTIR spectrometers, the optical path length modulation is achieved by using movable mirrors. The use of mechanical moving parts compromises the robustness of conventional FTIR systems. Efforts to create on-chip FTIR spectrometers have thus far focused on either direct miniaturization of conventional systems using micro-electromechanical system (MEMS) technologies [45], or tunable Mach–Zehnder Interferometers (MZI) based on electro-optic (EO) or thermo-optic (TO) effects [24]–[26]. Nevertheless, these devices exhibit much inferior performance compared to their conventional bulk counterparts due to the limited optical path length tuning range accessible on a chip. Table I compares the modulation efficiency of several optical path length modulation approaches, which is defined as the phase change (in radians) imparted on light wave
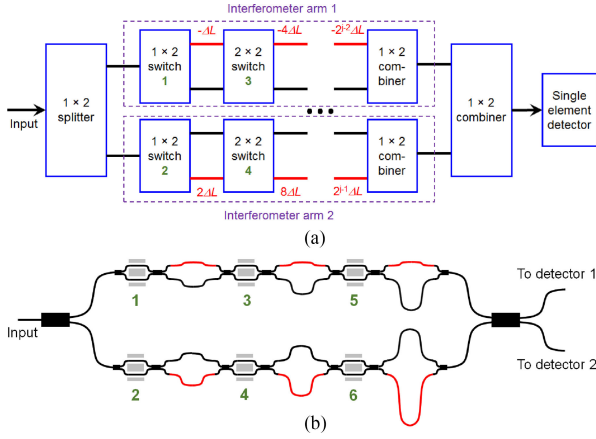
Fig. 8. (a) Block diagram of the dFTIR spectrometer design; (b) schematic layout of a 64-channel dFTIR spectrometer: the waveguide segments of varying lengths different from the standard length are shown in red (not drawn to scale). The green numbers label the 1×2 or 2×2 switches. Using two detectors at the interferometer output enables an improvement in the SNR by a factor of $\sqrt{2}$ in contrast to a 2×1 combiner with one detector [25].

per unit propagation length (in centimeters). Table I also lists the spectral resolution of a 1 cm long device near 1550 nm wavelength utilizing these modulation mechanisms calculated using (15).

Here we propose a novel spectrometer technology, digital Fourier Transform InfraRed (dFTIR), to overcome the aforementioned spectral resolution limit facing current on-chip spectrometers. The proposed spectrometer structure consists of an interferometer whose arms comprise a series of cascaded optical switches connected by waveguides of varying lengths. Unlike prior on-chip spectrometers where the arm length is changed by tuning the waveguide effective index, our approach modifies the optical path through which light propagates using the cascaded switches. Direct modification of the waveguide path is a far more effective approach for changing the optical path length than index modulation, as it is not bound by the small magnitude of index perturbation as is shown in Table I, thus enabling much improved spectral resolution.

The structure is illustrated in Fig. 8. Incident light entering the device is split into the two interferometer arms with optical switches to direct the light into an upper waveguide in the "UP" state or a lower waveguide in the "DOWN" state. The reference paths are shown in black in Fig. 8(a), while longer or shorter paths are shown in red. Each path in red is different from the black paths by a power of 2 times ΔL (ΔL being a pre-defined path length difference). As a result of this design, each permutation of the optical switches being "UP" or "DOWN" results in a different difference in optical path length between the two arms. Therefore, if there are 6 total switches as shown in Fig. 8(b), there are $2^6 = 64$ different interferometer configurations. Similarly, for j optical switches, the spectral channel number is:

$$N = 2^j \tag{16}$$

and the spectral resolution in wavenumbers is given by:

$$\delta\nu = \frac{1}{n_{\text{eff}} \cdot (2^j - 1) \cdot \Delta L} \sim \frac{1}{2^j} \cdot \frac{1}{n_{\text{eff}} \cdot \Delta L} \tag{17}$$

Component	Insertion loss	Footprint
SOI ridge waveguide [49]	1.2 dB/cm	0.5 μm (width) 0.22 μm (height)
Thermo-optic phase shifter [47]	0.23 dB	61.6 μm (length)
1×2 splitter/combiner [50]	0.28 dB	2 μm (length) 1.2 μm (width)
2×2 multi-mode interferometer [51]	0.15 dB	152 μm (length)

or:

$$\delta\lambda \sim \frac{1}{2^j} \cdot \frac{\lambda^2}{n_{\text{eff}} \cdot \Delta L} \tag{18}$$

where n_{eff} denotes the waveguide modal effective index. The spectral bandwidth in the wavelength domain is:

$$\text{BW} = \delta\lambda \cdot N \sim \frac{\lambda^2}{n_{\text{eff}} \cdot \Delta L}. \tag{19}$$

(16)–(19) suggest that performance scaling of the spectrometer can be readily achieved by increasing the number of switches j. To investigate the scaling behavior of the spectrometer, we consider an exemplary dFTIR device comprised of ridge waveguides and a total of j thermo-optic switches, both fabricated in a silicon-on-insulator (SOI) platform. Key performance specifications of SOI photonic components assumed in this analysis are summarized in Table II. We note that the numbers in Table II are quoted for devices processed in commercial multi-project-wafer (MPW) runs, which are representative of state-of-the-art photonic manufacturing in a production-relevant setting. To obtain sub-nm spectral resolution, the maximum path length difference between the two interferometer arms $2^j \Delta L$ should be in the order of several millimeters or more. Therefore, the thermo-optic switches and the splitters/combiners have negligible contributions to the overall device footprint. Each set of two optical switches, such as 1 and 2 in Fig. 8(b), form a "stage". The black reference arms in each "stage" are constrained by the condition that the shorter arm lengths (the red paths labeled with negative numbers) have to be greater than zero, which gives the reference arm length (in μm) as:

$$L_{\text{tot}} = (\Delta L + 4\Delta L + 16\Delta L... + 2^{j-2}\Delta L)$$
$$+ \frac{j}{2} \cdot L_{\text{PS}} + (j-1) \cdot L_{2\times2} + 4 \cdot L_{1\times2}$$
$$\sim \frac{2^j}{3}\Delta L + j \cdot 182.8 - 144 \tag{20}$$

where $L_{\text{PS}} = 61.6$ μm, $L_{2\times2} = 152$ μm, and $L_{1\times2} = 2$ μm based on the component specifications listed in Table II. The total insertion loss (IL, given in dB) is:

$$\text{IL} = \frac{j}{2} \cdot \text{IL}_{\text{PS}} + (j-1) \cdot \text{IL}_{2\times2} + 4 \cdot \text{IL}_{1\times2} + \frac{2^j}{3}\Delta L \cdot \text{IL}_{\text{WG}}$$
$$= j \cdot 0.265 + 0.97 + \frac{2^j}{3}\Delta L \cdot 1.2 \times 10^{-4} \tag{21}$$

where $\text{IL}_{\text{PS}} = 0.23$ dB, $\text{IL}_{2\times2} = 0.15$ dB, $\text{IL}_{1\times2} = 0.28$ dB, and $\text{IL}_{\text{WG}} = 1.2 \times 10^{-4}$ dB/cm.
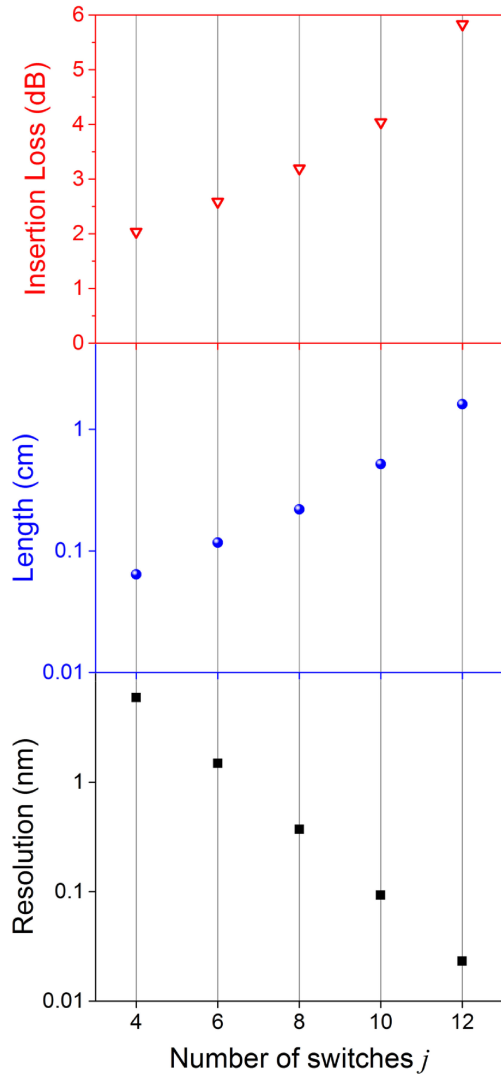
Fig. 9.   Projected spectral resolution, interferometer arm length and insertion loss of the dFTIR spectrometer according to (16)–(21).

Now we examine a specific example of an on-chip spectrum analyzer covering the entire C and L bands (1530–1625 nm wavelengths). Here we use $n_{\text{eff}} = 2.55$, $\lambda = 1577.5$ nm, and $\Delta L = 10.3$ μm. Fig. 9 plots the performance projections of the spectrometer. Taking $j = 12$, (16)–(21) yield BW = 95 nm, $\delta\lambda = 0.023$ nm, IL = 5.8 dB, and $L_{\text{tot}} = 1.6$ cm. These performance specifications are superior compared to commercial C/L band optical channel monitors [52]. Additionally, the waveguides in the interferometer arms can be folded into a zig-zag or spiral pattern to reduce the device footprint if necessary.

Last but not least, it is also worth noting that the spectrometer design is highly tolerant against fabrication errors such as component cross-sectional dimension or length deviations. To counter such fabrication errors, a calibration step can be performed prior to using the device for spectroscopic interrogations. Calibration data will assume the form of a $2^j \times 2^j$ matrix. Each column of the matrix gives the transmittance through the spectrometer at different switch "UP"/"DOWN" state combinations, whereas each row of the matrix specifies the device transmittance at a particular "UP"/"DOWN" state configuration of the switches. The spectrograph of an arbitrary polychromatic input can be solved by recording the transmittance at all 2^j distinctive combinations of the switch "UP"/"DOWN" states, and multiplying the resulting vector with the inverse of the calibration matrix. For the same reason, operation bandwidth of the spectrometer is only limited by the single mode condition of the waveguides comprising the spectrometer rather than the operation bandwidth of the optical switches or the beam splitters/combiners, as high contrast ratio of the switches is not required to solve the spectrograph once the calibration matrix is measured. We further note that the calibration matrix is invariant for a given spectrometer device and therefore the calibration step only needs to be carried out once, and the calibration data can be stored for subsequent measurements.

V. CONCLUSION AND FUTURE OUTLOOK

In this paper, we highlighted the challenges associated with on-chip integration of infrared spectroscopic sensors, in particular, performance penalties resulting from device size downscaling. To resolve these challenges, we discussed two sensor designs uniquely capable of reaping performance benefits from scaling. In the first example, tight optical and thermal confinement in microphotonic devices lead to a gigantic photothermal sensitivity boost compared to the sensitivity of traditional absorption spectroscopic sensors. In the second case, we proposed a new on-chip Fourier Transform InfraRed spectrometer design leveraging two functions made available in compact, chip-scale platforms through photonic integration: optical switching and long, folded optical paths. In both cases we have shown that on-chip spectroscopic sensors can attain performance metrics comparable to or even superior to conventional bulk optical instruments.

Fabrication and characterization of these spectroscopic sensors are currently underway and will be presented in follow-up publications.

REFERENCES

[1] B. Stuart, *Infrared Spectroscopy*. New York, NY, USA: Wiley, 2005.
[2] G. Overton, "How spectrometers have shrunk and grown since 2010," *Laser Focus World*, vol. 52, no. 2, pp. 35–41, 2016.
[3] S. W. Sharpe *et al.*, "Gas-phase databases for quantitative infrared spectroscopy," *Appl. Spectroscopy*, vol. 58, no. 12, pp. 1452–1461, 2004.
[4] J. F. Bauters *et al.*, "Planar waveguides with less than 0.1 dB/m propagation loss fabricated with wafer bonding," *Opt. Express*, vol. 19, no. 24, pp. 24 090–24 101, 2011.
[5] D. R. Herriott and H. J. Schulte, "Folded optical delay lines," *Appl. Opt.*, vol. 4, no. 8, 1965, Art. no. 883.
[6] A. Z. Subramanian *et al.*, "Silicon and silicon nitride photonic circuits for spectroscopic sensing on-a-chip," *Photon. Res.*, vol. 3, no. 5, 2015, Art. no. B47. [Online]. Available: https://www.osapublishing.org/abstract.cfm?URI=prj-3-5-B47
[7] W. Bogaerts *et al.*, "Silicon-on-insulator spectral filters fabricated with CMOS technology," *IEEE J. Sel. Topics Quantum Electron.*, vol. 16, no. 1, pp. 33–44, Jan./Feb. 2010.
[8] G. Roelkens *et al.*, "Silicon-based heterogeneous photonic integrated circuits for the mid-infrared," *Opt. Mater. Express*, vol. 3, no. 9, 2013, Art. no. 1523. [Online]. Available: http://www.opticsinfobase.org/abstract.cfm?URI=ome-3-9-1523

[9] S. Babin *et al.*, "Digital optical spectrometer-on-chip," *Appl. Phys. Lett.*, vol. 95, no. 4, pp. 1–4, 2009.

[10] M. Florjańczyk *et al.*, "Multiaperture planar waveguide spectrometer formed by arrayed Mach-Zehnder interferometers," *Opt. Express*, vol. 15, no. 26, pp. 18 176–18 189, 2007.

[11] Z. Xia *et al.*, "High resolution on-chip spectroscopy based on miniaturized microdonut resonators," *Opt. Express*, vol. 19, no. 13, pp. 12 356–12 364, 2011.

[12] F. Civitci, M. Hammer, and H. Hoekstra, "Planar prism spectrometer based on adiabatically connected waveguiding slabs," *Opt. Commun.*, vol. 365, pp. 29–37, 2016. [Online]. Available: http://linkinghub.elsevier.com/retrieve/pii/S0030401815303217

[13] R. G. DeCorby, N. Ponnampalam, E. Epp, T. Allen, and J. N. McMullin, "Chip-scale spectrometry based on tapered hollow Bragg waveguides," *Opt. Express*, vol. 17, no. 19, pp. 16632–16645, 2009. [Online]. Available: http://www.ncbi.nlm.nih.gov/pubmed/19770879

[14] X. Gan, N. Pervez, I. Kymissis, F. Hatami, and D. Englund, "A high-resolution spectrometer based on a compact planar two dimensional photonic crystal cavity array," *Appl. Phys. Lett.*, vol. 100, no. 23, 2012, Art. no. 231104.

[15] M. J. E. Golay, "Multi-Slit Spectrometry," *J. Opt. Soc. Amer.*, vol. 39, no. 6, pp. 437–444, 1949.

[16] B. Redding, S. F. Liew, R. Sarma, and H. Cao, "Compact spectrometer based on a disordered photonic chip," *Nature Photon.*, vol. 7, no. 9, pp. 746–751, 2013.

[17] N. H. Wan *et al.*, "High-resolution optical spectroscopy using multimode interference in a compact tapered fibre," *Nature Commun.*, vol. 6, 2015, Art. no. 7762. [Online]. Available: http://www.nature.com/doifinder/10.1038/ncomms8762

[18] J. Bao and M. G. Bawendi, "A colloidal quantum dot spectrometer," *Nature*, vol. 523, pp. 67–70, 2015.

[19] E. le Coarer *et al.*, "Wavelength-scale stationary-wave integrated Fourier-transform spectrometry," *Nature Photon.*, vol. 1, no. 8, pp. 473–478, 2007. [Online]. Available: http://dx.doi.org/10.1038/nphoton.2007.138

[20] B. Redding, S. M. Popoff, and H. Cao, "All-fiber spectrometer based on speckle pattern reconstruction," *Opt. Express*, vol. 21, no. 5, 2013, Art. no. 6584. [Online]. Available: http://www.ncbi.nlm.nih.gov/pubmed/23482230

[21] B. Redding and H. Cao, "Using a multimode fiber as a high-resolution, low-loss spectrometer," *Opt. Lett.*, vol. 37, no. 16, 2012, Art. no. 3384.

[22] M. E. Gehm *et al.*, "Static two-dimensional aperture coding for multimodal, multiplex spectroscopy," *Appl. Opt.*, vol. 45, no. 13, pp. 2965–2974, 2006.

[23] Z. Xu *et al.*, "Multimodal multiplex spectroscopy using photonic crystals," *Opt. Express*, vol. 11, no. 18, pp. 2126–2133, 2003.

[24] R. G. Sellar and G. D. Boreman, "Comparison of relative signal-to-noise ratios of different classes of imaging spectrometer," *Appl. Opt.*, vol. 44, no. 9, pp. 1614–1624, 2005.

[25] M. Harwit, *Hadamard Tranform Optics*. Amsterdam, The Netherlands: Elsevier, 1979.

[26] T. H. Chao *et al.*, "Compact liquid crystal waveguide based Fourier transform spectrometer for in-situ and remote gas and chemical sensing - art. no. 69770P," in *Proc. Int. Conf. Opt. Instrum. Technol.: Adv. Sensor Technol. Appl.*, 2009, vol. 7508, pp. 1–11.

[27] B. Dong *et al.*, "Nano-Silicon-Photonic Fourier Transform Infrared (FTIR)," *OSA Technical Digest (online) (Optical Society of America)* vol. 1, pp. 3–4, 2015.

[28] Y. Dattner and O. Yadid-Pecht, "Fully Integrated Complementary Metal Oxide Semiconductor (CMOS) Fourier Transform Infrared (FTIR) Spectrometer and Raman Spectrometer," U.S. Patent 2013/0321816 A1, 2013.

[29] Y. Chen, H. Lin, J. Hu, and M. Li, "Heterogeneously integrated silicon photonics for the Mid-Infrared and spectroscoping sensing," *ACS Nano*, vol. 8, no. 7, pp. 6955–6961, 2014.

[30] J. Hu *et al.*, "Cavity-enhanced infrared absorption in planar chalcogenide glass microdisk resonators: Experiment and analysis," *J. Lightw. Technol.*, vol. 27, no. 23, pp. 5240–5245, 2009.

[31] C. J. Smith *et al.*, "Sensing nitrous oxide with QCL-coupled silicon-on-sapphire ring resonators," *Opt. Express*, vol. 23, no. 5, Feb. 2015, Art. no. 5491. [Online]. Available: http://www.opticsinfobase.org/viewmedia.cfm?uri=oe-23-5-5491&seq=0% &html=true

[32] A. Nitkowski, L. Chen, and M. Lipson, "Cavity-enhanced on-chip absorption spectroscopy using microring resonators," *Opt. Express*, vol. 16, no. 16, Jul. 2008, Art. no. 11930. [Online]. Available: http://www.opticsinfobase.org/abstract.cfm?URI= oe-16-16-11930

[33] A. Nitkowski, A. Baeumner, and M. Lipson, "On-chip spectrophotometry for bioanalysis using microring resonators," *Biomed. Opt. Express*, vol. 2, no. 2, pp. 271–277, Jan. 2011.

[34] V. Singh *et al.*, "Mid-infrared materials and devices on a Si platform for optical sensing," *Sci. Technol. Adv. Mater.*, vol. 15, no. 1, 2014, Art. no. 014603.

[35] J. Hu, "Ultra-sensitive chemical vapor detection using micro-cavity photothermal spectroscopy," *Opt. Express*, vol. 18, no. 21, pp. 22 174–22 186, Oct. 2010. [Online]. Available: http://www.ncbi.nlm.nih.gov/pubmed/20941119

[36] H. Lin, Z. Yi, and J. Hu, "Double resonance 1-D photonic crystal cavities for single-molecule mid-infrared photothermal spectroscopy: theory and design," *Opt. Lett.*, vol. 37, no. 8, pp. 1304–1306, Apr. 2012. [Online]. Available: http://www.ncbi.nlm.nih.gov/pubmed/22513667

[37] T. Carmon, L. Yang, and K. J. Vahala, "Dynamical thermal behavior and thermal self-stability of microcavities," *Opt. Express*, vol. 12, no. 20, pp. 654–656, 2004.

[38] K. P. Birch and M. J. Downs, "An updated Edlen equation for the refractive index of air," *Metrologia*, vol. 30, pp. 155–162, 1993.

[39] W. F. Herget, W. E. Deeds, N. M. Gailar, R. J. Lovell, and A. H. Nielsen, "Infrared spectrum of hydrogen Fluoride: Line positions and line shapes part II treatment of data and results," *J. Opt. Society Amer.*, vol. 52, no. 10, 1962, Art. no. 1113.

[40] L. Petit *et al.*, "Compositional dependence of the nonlinear refractive index of new germanium-based chalcogenide glasses," *J. Solid State Chem.*, vol. 182, no. 10, pp. 2756–2761, 2009. [Online]. Available: http://dx.doi.org/10.1016/j.jssc.2009.07.027

[41] J. T. Robinson, K. Preston, O. Painter, and M. Lipson, "First-principle derivation of gain in high-index- contrast waveguides," *Opt. Express*, vol. 16, no. 21, pp. 16 659–16 669, 2008.

[42] Q. Du *et al.*, "Low-loss photonic device in Ge Sb S chalcogenide glass," *Opt. Lett.*, vol. 41, no. 13, pp. 3090–3093, 2016.

[43] "VPL molecular spectroscopic database," 2008 [Online]. Available: http://vpl.astro.washington.edu/spectra/hf.htm

[44] V. S. Shiryaev *et al.*, "Preparation of optical fibers based on Ge-Sb-S glass system," *Opt. Mater.*, vol. 32, no. 2, pp. 362–367, 2009. [Online]. Available: http://dx.doi.org/10.1016/j.optmat.2009.09.003

[45] L. P. Schuler, J. S. Milne, J. M. Dell, and L. Faraone, "MEMS-based microspectrometer technologies for NIR and MIR wavelengths," *J. Phys. D: Appl. Phys.*, vol. 42, no. 13, 2009, Art. no. 133001.

[46] H. Xu *et al.*, "High speed silicon Mach-Zehnder modulator based on interleaved PN junctions," *Opt. Express*, vol. 20, no. 14, pp. 15 093–15 099, 2012. [Online]. Available: http://www.ncbi.nlm.nih.gov/pubmed/22772206

[47] N. C. Harris *et al.*, "Efficient , compact and low loss thermo-optic phase shifter in silicon," *Opt. Express*, vol. 22, no. 9, pp. 83–85, 2014.

[48] T. Ako *et al.*, "Electrically tuneable lateral leakage loss in liquid crystal clad shallow-etched silicon waveguides," *Opt. Express*, vol. 23, no. 3, pp. 2846–2856, 2015.

[49] T. Baehr-Jones, "OpSIS-IME OI50 process—Performance summary," OpSIS Center, University of Delaware, Newark, DE, Tech. Rep. [Online]. Available: http://opsisfoundry.org/wp-content/uploads/opsis_oi50_performance_summary_10_8_13.pdf

[50] Y. Zhang *et al.*, "A compact and low loss Y-junction for submicron silicon waveguide," *Opt. Express*, vol. 21, no. 1, pp. 1310–1316, 2013. [Online]. Available: http://www.ncbi.nlm.nih.gov/pubmed/23389024

[51] P. Dumais *et al.*, "2 × 2 Multimode Interference Coupler with Low Loss Using 248 nm Photolithography," in *Optical Fiber Communication Conference, OSA Technical Digest (online) (Optical Society of America)*, pp. 19–21, 2016.

[52] "Optical channel monitor based on planar lightwave circuit technology," Enablence, Ottawa, ON, Canada, Tech. Rep., pp. 1–4, 2010. [Online]. Available: http://www.enablence.com/technologies/wp-content/uploads/2013/07/Datasheet_OCSD_OCM_PLC.pdf

Derek M. Kita received the B.S. degree in both physics and materials science and engineering from the Massachusetts Institute of Technology (MIT) in Cambridge, MA, USA, in 2014, Since then, he has been working toward the Ph.D. degree in materials science and engineering at MIT. His research focuses on integrated microphotonics in the mid-infrared for spectroscopy and chemical sensing.

Hongtao Lin received the B.S. degree in materials physics from University of Science and Technology of China, Hefei, China, in 2010, and the Ph.D. degree in materials science from University of Delaware, Newark, NJ, USA, in 2015.

Since 2015, he has been a Postdoctoral Associate in the Department of Materials Science and Engineering at the Massachusetts Institute of Technology, Cambridge, MA, USA. His research interests include chalcogenide glass photonics, optical communications, mid-infrared sensing, and flexible photonics.

Anu Agarwal received the doctoral degree in electrical engineering from Boston University, Boston, MA, USA, in 1994, where she investigated the spatial extent of point defect interactions in silicon. She has been at Massachusetts Institute of Technologys Microphotonics Center since 1994, except for a short (2001–2004) stint at Clarendon Photonics, where she was a part of a team of engineers developing a novel optical filter. She is currently a Principal Research Scientist, she is developing integrated Si-CMOS compatible linear and nonlinear materials for photonic devices, especially in the mid-infrared regime, for hyperspectral imaging and chem-bio sensing because most chemical and biological toxins have their fingerprints in this range. She has more than 100 journal and refereed conference publications, 6 awarded patents, and 5 pending patents. Her work on mid-infrared materials and devices is creating a planar, integrated, Si-CMOS-compatible microphotonics platform which will enable on-chip imaging and sensing applications.

Kathleen Richardson is currently a Professor of optics and materials science and engineering at University of Central Florida College of Optics and Photonics, Orlando, FL, USA, where she runs the Glass Processing and Characterization Laboratory. Most recently at Clemson University where she served as Director of the School of Materials Science and Engineering (2005–2010), she and her research team carry out synthesis and characterization of novel glass and glass ceramic materials for optical applications, examining the role of structure/property relationships on resulting optical function and performance in bulk, planar, and fiber optical materials. Her group has extensive industrial and government supported research programs evaluating materials for precision molded optics, the use of nonoxide glasses in chem-bio planar sensors in diverse environments, evaluation of complex material interactions in next-generation integrated opto-electronic chip design, and in the design and fabrication of nano-composite materials and devices for advanced detection and optical applications.

Her group is a leading source of expertise in the evaluation of photo-/radiation induced structure/property modification mechanisms in nonoxide glasses for optical applications. She has authored more than 220 peer-reviewed publications, numerous proceedings, and book chapters, and has organized and chaired multiple domestic and international meetings within her discipline.

Dr. Richardson is currently the Past-President of the American Ceramic Society (ACerS), the past-Chair of ACerS Glass and Optical Materials Division, and the Past-President of the National Institute of Ceramic Engineers. She has just completed a term as a Member of the Board of Directors of the Society of Photo-Optical Instrumentation Engineers and currently serves on the Coordinating Technical Committee of the International Commission on Glass. She has previously served on advisory boards of numerous organizations, including the Board of Directors of the ACerS, Virginia Techs Materials Science and Engineering Department, the NSF-ERC on Mid-Infrared Technologies for Health and the Environment at Princeton University, and as part of the Australian Research Councils Centre of Excellence for Ultrahigh-bandwidth Devices for Optical Systems, in Sydney, Australia. She is a recognized World Leader in infrared glass research and education, and as a result of these efforts, currently holds the rank of Fellow, in the ACerS, the Society of Glass Technology, U.K., SPIE, and the Optical Society of America. Since 2006, she has served as a Member of the Board of Trustees at Alfred University.

Igor Luzinov received the M.S. degree in chemical engineering and technology and the Ph.D. degree in polymer chemistry from Lviv Polytechnic National University, Ukraine, in 1985 and 1990, respectively. He is currently a Professor of materials science and engineering at Clemson University, Clemson, SC, USA. Prior to joining the faculty of Clemson University, he served as a Senior Research Scientist at Physical Chemistry Institute, National Academy of Sciences of Ukraine, NATO Research Fellow at Center Education and Research on Macromolecules, University of Liege, Belgium, and Postdoctoral Research Associate at Iowa State and Western Michigan Universities.

Tian Gu received the B.S. degree in electrical engineering from the Beijing Institute of Technology, Beijing, China, in 2004, and the Ph.D. degree in electrical and computer engineering from the University of Delaware, Newark, NJ, USA, in 2012.

He is currently a Research Scientist of Materials Science and Engineering at Massachusetts Institute of Technology, Cambridge, MA, USA. His research interests are focused on optical sensing, micro-scale photovoltaics, flexible photonics, photonic integrated circuits, and imaging.

Dr. Gu received the R&D 100 Award in 2012. He serves as a Program Committee Member for the IEEE Photonics Society Optical Interconnects Conference.
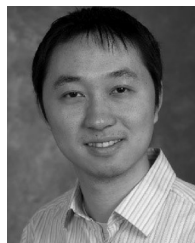
Juejun (JJ) Hu received the B.S. degree from Tsinghua University, China, in 2004, and the Ph.D. degree from Massachusetts Institute of Technology, Cambridge, MA, USA, in 2009, both in materials science and engineering. He is currently the Merton C. Flemings Career Development Associate Professor at MITs Department of Materials Science and Engineering. His primary research interest is enhanced photonmatter interactions in nanophotonic structures, with an emphasis on on-chip spectroscopy and chemical sensing applications using novel infrared glasses. Prior to joining MIT, he was an Assistant Professor at the University of Delaware from 2010 to 2014.

Hu has authored and coauthored more than 60 refereed journal publications since 2006 and has been awarded six U.S. patents. He has been recognized with the National Science Foundation Faculty Early Career Development award, the Gerard J. Mangone Young Scholars Award, the University of Delaware College of Engineering Outstanding Junior Faculty Member, the University of Delaware Excellence in Teaching Award, among others.

Dr. Hu is currently the Deputy Editor of the OSA journal Optical Materials Express, and he is a Member on technical program committees for conferences including MRS, CLEO, OSA Congress, ACerS GOMD, ICG, and others.